Frontiers of Information Technology & Electronic Engineering
www.jzus.zju.edu.cn; engineering.cae.cn; www.springerlink.com
ISSN 2095-9184 (print); ISSN 2095-9230 (online)
E-mail: jzus@zju.edu.cn

Compact input-reflectionless balanced bandpass filter with flexible bandwidth using three-line coupled structure*

Yahui ZHU[1,2], Jing CAI[1,2], Wei QIN[1,2], Wenwen YANG[1,2], Jianxin CHEN[†‡1,2]

[1]*School of Information Science and Technology, Nantong University, Nantong 226019, China*

[2]*Research Center for Intelligent Information Technology, Nantong University, Nantong 226019, China*

[†]E-mail: jjxchen@hotmail.com

Received June 18, 2022; Revision accepted Oct. 30, 2022; Crosschecked Nov. 28, 2022

Abstract: A compact input-reflectionless balanced bandpass filter (BPF) with flexible bandwidth (BW) using a three-line coupled structure (TLCS) is presented in this paper. For the differential mode (DM), the TLCS is applied to achieve the bandpass response; meanwhile, the input coupled-feed line of the TLCS is reused in the input absorption network. This design shows a good fusion of the absorptive and BPF sections, effectively reducing the circuit size, and the BWs of the two sections that can be controlled separately result in a flexibly controllable DM response BW of the proposed input-reflectionless balanced BPF. Detailed analyses of the ratio of the two-part BWs have been given for the first time, which is vital for the passband flatness and reflectionless feature. In the codesign of this work, the input-reflectionless DM bandpass response can be optimized easily, while wideband common mode (CM) noise absorption is achieved by the input absorption network. To verify the design method, a prototype with a compact layout ($0.52\lambda \times 0.36\lambda$) is designed and measured in the 0–7.0 GHz range. The DM center frequency (f_0) is 2.45 GHz with a measured 3 dB fractional bandwidth of 31.4%. The simulation and measurement results with good agreement are presented, showing good performance, e.g., low insertion loss (0.43 dB), wide upper stopband for the DM bandpass response (over 20 dB rejection level up to $2.72f_0$), and wideband DM reflectionless and CM noise absorption (fractional absorption bandwidth of 285.7%).

Key words: Input-reflectionless filter; Balanced bandpass filter (BPF); Differential mode (DM); Common mode (CM); Three-line coupled structure (TLCS)
https://doi.org/10.1631/FITEE.2200261 **CLC number:** TN015

1 Introduction

Balanced devices have attracted immense attention due to the urgent requirement of immunity to environmental noise, electromagnetic interference, and crosstalk (Zhou and Chen, 2017). On this basis, with the development of chip technology, many balanced circuits have been conceived, such as couplers (Feng et al., 2019; Li HY et al., 2019; Zhang ZQ et al., 2021), power dividers (Shi et al., 2016; Xu et al., 2019; Yu et al., 2022), diplexers (Li YC et al., 2020; Song et al., 2020), and antennas (Cao et al., 2020; Kou et al., 2022; Wang et al., 2022). As an important frequency selection component in radio frequency (RF)/microwave circuits and systems, the balanced implementation of the bandpass filter (BPF) is also very important (Chen JX et al., 2016; Bi et al., 2020; Feng et al., 2021; Wu DS et al., 2022). For these works, desirable common mode (CM) rejection, sharp differential mode (DM) roll-off skirt, and compact layout are competitive indicators, and they have been widely considered. However, the stability of the operating system would inevitably be deteriorated by the

‡ Corresponding author
* Project supported by the National Natural Science Foundation of China (No. 20201438)
ORCID: Yahui ZHU, https://orcid.org/0000-0003-0230-8271; Jianxin CHEN, https://orcid.org/0000-0002-8703-5294

unwanted DM signals and CM noise returning to the source. This issue has attracted ever-increasing attention.

Although the traditional adoption of isolators or attenuators alleviates the interference due to undesired reflected signals, it also leads to an inevitable increase in size and insertion loss (IL) (Lee B et al., 2022). Accordingly, the reflectionless technique has been explored recently; it can dissipate the reflected interference energy inside instead of returning it to the source (Morgan and Boyd, 2015; Han et al., 2022). Consequently, a large number of single-ended reflectionless filters have been reported (Morgan and Boyd, 2015; Gómez-García et al., 2019; Guilabert et al., 2019; Morgan et al., 2019; Wu XH et al., 2020; Fan et al., 2021a, 2021b; Lee J et al., 2021; Xu et al., 2022; Zhu YH et al., 2022). Based on this, balanced BPFs with different types have been developed in recent years (Zhang WW et al., 2017; Gómez-García et al., 2018; Lin et al., 2019; Lin and Wu, 2020; Yang et al., 2020; Zhu Y et al., 2020; Chen X et al., 2021; Zhang YF et al., 2022) because balanced topology has become popular in modern circuits and systems (Chen JX et al., 2016; Shi et al., 2016; Zhou and Chen, 2017; Feng et al., 2019, 2021; Li HY et al., 2019; Xu et al., 2019; Bi et al., 2020; Cao et al., 2020; Li YC et al., 2020; Song et al., 2020; Zhang ZQ et al., 2021; Kou et al., 2022; Wang et al., 2022; Wu DS et al., 2022; Yu et al., 2022).

As a common method in the implementation of single-ended reflectionless behavior, the topology of complementary diplexer based behavior (Gómez-García et al., 2019; Wu XH et al., 2020; Fan et al., 2021a, 2021b; Xu et al., 2022; Zhu YH et al., 2022) is used in balanced planar BPFs with symmetrical DM quasi-reflectionless characteristics (Gómez-García, et al., 2018). The multilayered vertical transition structure is adopted (Yang et al., 2020) to realize the wideband input-reflectionless response of the DM BPF, and its out-of-band DM signals are dissipated by resistively terminated microstrip branches. In addition, for CM absorption, symmetrically loaded resistors are used (Zhang WW et al., 2017; Lin et al., 2019; Lin and Wu, 2020; Zhu Y et al., 2020). The developed balanced BPFs with the characteristic of wideband CM noise absorption are introduced (Lin and Wu, 2020; Zhu Y et al., 2020). Although some efforts have been made to absorb DM signals or CM noise, the absorption of unwanted DM and CM signals is rarely considered at the same time. Recently, balanced BPFs (Chen X et al., 2021; Zhang YF et al., 2022) with both DM reflectionless and CM absorption have been reported. However, the large size is a problematic issue. For example, multiple absorption networks in parallel with multiple bandpass sections shown in Fig. 1a result in a large size, although the filtering performance is improved (Chen X et al., 2021). However, the limitation of the DM absorptive bandwidth (BW) still exists because of the mismatch in the out-of-band operating ranges. Obviously, it is still a challenge to achieve a balanced BPF that can absorb both DM reflected signals and CM noise with large absorption BW and miniaturized size simultaneously.

To solve the above-mentioned problems, we present an input-reflectionless balanced BPF using the synthesis method. It has the advantages of compact layout and high performance by taking the absorptive section (ABSS) and the BPF section into account simultaneously in a codesign procedure, as shown in Fig. 1b. The shared transmission line (STL) acts not only as a key part of the ABSS but also as a coupled-feed line (CFL) of the BPF section based on the three-line coupled structure (TLCS). The relationship between the passband BW of the input-reflectionless balanced BPF and the BWs of the ABSS and BPF section is discussed. This has not been mentioned in detail before, in either diplexer-based single-end or balanced design (Zhang WW et al., 2017; Gómez-García et al., 2018, 2019; Lin et al., 2019; Lin and Wu, 2020; Wu XH et al., 2020; Yang et al., 2020; Zhu Y et al., 2020; Chen X et al., 2021; Fan et al., 2021a, 2021b; Xu et al., 2022; Zhang YF et al., 2022; Zhu YH et al., 2022). Meanwhile, the BW design procedure of the proposed input-reflectionless balanced BPF is given. In addition, the ratio of the two-part BWs and its vital effect on the reflectionless performance and DM passband flatness are analyzed in detail, which has important implications for the diplexer-based reflectionless BPF designs. Accordingly, the seamless integration of ABSS and TLCS-based BPF section provides a compact layout while maintaining good DM filtering performance (such as low IL and a wide upper stopband) and wideband reflectionless for both DM and CM.

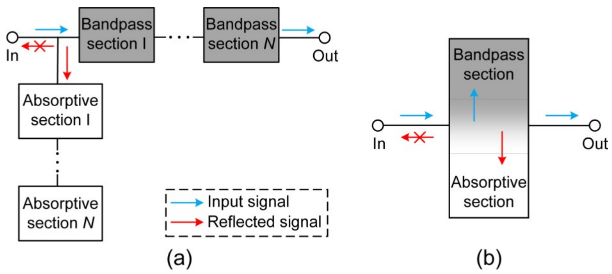

Fig. 1 Conceptual operation mechanism of the input-reflectionless bandpass filter: (a) traditional cascaded system; (b) fusion design method

2 Theoretical analysis and design

The schematic layout of the proposed input-reflectionless balanced BPF is shown in Fig. 2. The whole circuit is symmetrical with respect to plane AA'. It consists of a pair of symmetrical TLCS-based BPFs and absorption networks, in which a pair of STLs are reused, with the electrical lengths of all coupled lines and transmission lines being equal to π/2 (quarter waveguide wavelength: λ/4), i.e., $\theta_a=\theta_b=\theta_c=\theta_d=\pi/2$ at the center frequency (f_0=2.45 GHz). Figs. 3a and 3b show the DM and CM bisected equivalent circuits of the proposed input-reflectionless balanced BPF, respectively. Detailed theoretical analysis and working mechanism are illustrated as follows.

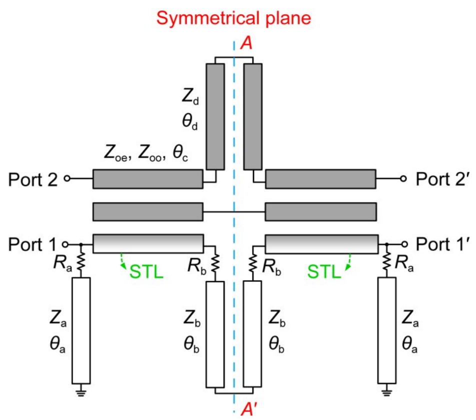

Fig. 2 Schematic of the proposed input-reflectionless balanced bandpass filter

2.1 Differential mode analysis

The DM bisected equivalent circuit of the proposed input-reflectionless balanced BPF is shown in Fig. 3a. It can be divided into two parts for analysis, i.e., ABSS and BPF section.

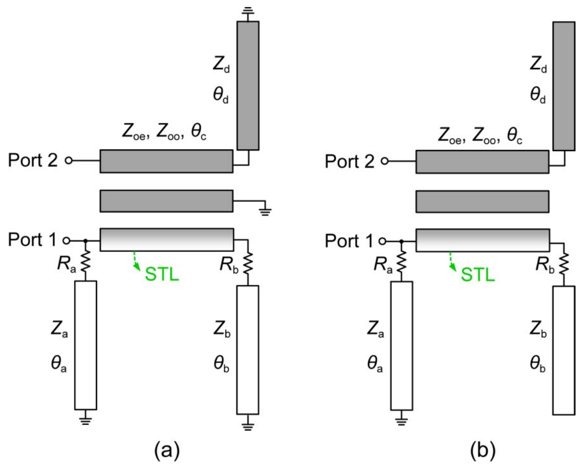

Fig. 3 Equivalent circuits: (a) differential mode; (b) common mode

2.1.1 Absorptive section

For the absorption network, ABSS with double lossy stubs is given in Fig. 4, consisting of a λ/4 STL with characteristic impedance Z_c and two λ/4 lossy stubs with characteristic impedances Z_a and Z_b. The λ/4 lossy stubs can be regarded as transparent at f_0; hence, the stopband at f_0 is provided by the STL. In contrast, the out-of-band energy can be absorbed by the lossy resistors (R_a and R_b). For the ABSS in Fig. 4, the input impedance Z_{in1} and the reflection coefficient $|S_{11}|$ can be given as

$$Z_{\mathrm{in1}}=(R_a+\mathrm{j}Z_a\tan\theta_a) \,//\, \frac{Z_c\left[R_b+\mathrm{j}(Z_b\tan\theta_b+Z_c\tan\theta_c)\right]}{(Z_c-Z_b\tan\theta_b\tan\theta_c)+\mathrm{j}R_b\tan\theta_c}, \tag{1}$$

$$|S_{11}|=20\lg\left|\frac{Z_{\mathrm{in1}}-Z_0}{Z_{\mathrm{in1}}+Z_0}\right|(\mathrm{dB}), \tag{2}$$

where Z_0 is the port reference impedance.

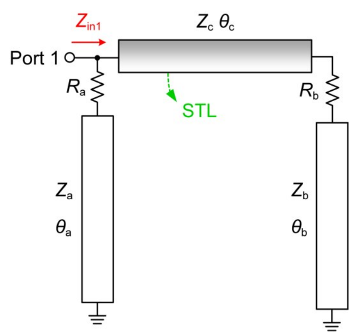

Fig. 4 Schematic of the proposed absorptive section with double lossy stubs

Fig. 5 shows the curves of the proposed ABSS with various parameters. As illustrated in Figs. 5a–5f, the values of Z_a, Z_b, and Z_c affect the BW of the reflected signals (when Z_{in1}=0, the reflection coefficient $|S_{11}|$=0 dB). Figs. 5e and 5f show that Z_c is the primary influencing factor to determine the reflection BW of the ABSS (BW_{ABSS}, i.e., $|S_{11}|$>−10 dB) in Fig. 4, and a higher Z_c can develop a smaller reflection BW. As Z_c increases, the variation trend of reflection BW tends to be flat, but the mismatch (i.e., the difference between the value of Z_{in1} and 50 Ω) near f_0 rises sharply. In addition, the matching performance is affected by Z_a and R_b. A lower mismatch near f_0 can be obtained by a smaller value of Z_a. In addition, as plotted in Figs. 5g and 5h, the matching performances near f_0 and at the second harmonic ($2f_0$) are highly dependent on R_b, and they increase simultaneously as R_b increases. The absorption resistor R_a assembled at the input port 1 is equal to Z_0 to achieve wideband CM reflectionless performance, which will be discussed in Section 2.2.

2.1.2 Bandpass filter section

For the BPF section, a compact and easy-to-integrate TLCS is used. The configuration of the TLCS-based BPF is shown in Fig. 6a. The widths of the CFLs and the center $\lambda/4$ resonator are w_c and w_0, respectively. The gap between them is s. For simplicity, the three coupled lines are regarded as having equal widths (w_0=w_c). The impedance matrix (Z-matrix) of this six-port network is given by (Yamamoto et al., 1966)

$$\begin{bmatrix} V_1 \\ V_2 \\ V_3 \\ V_4 \\ V_5 \\ V_6 \end{bmatrix} = \begin{bmatrix} E\alpha & F\alpha & G\alpha & G\beta & F\beta & E\beta \\ F\alpha & E\alpha & F\alpha & F\beta & E\beta & F\beta \\ G\alpha & F\alpha & E\alpha & E\beta & F\beta & G\beta \\ G\beta & F\beta & E\beta & E\alpha & F\alpha & G\alpha \\ F\beta & E\beta & F\beta & F\alpha & E\alpha & F\alpha \\ E\beta & F\beta & G\beta & G\alpha & F\alpha & E\alpha \end{bmatrix} \begin{bmatrix} I_1 \\ I_2 \\ I_3 \\ I_4 \\ I_5 \\ I_6 \end{bmatrix}, \tag{3}$$

where

$$\begin{cases} E\alpha = [-\mathrm{j}(Z_{oe} + Z_{oo})\cot\theta]/2, \\ F\alpha = [-\mathrm{j}(Z_{oe} - Z_{oo})\cot\theta]/2, \\ E\beta = [-\mathrm{j}(Z_{oe} + Z_{oo})\csc\theta]/2, \\ F\beta = [-\mathrm{j}(Z_{oe} - Z_{oo})\csc\theta]/2, \\ G\alpha = [-\mathrm{j}k_{cc}(Z_{oe} - Z_{oo})\cot\theta]/2, \\ G\beta = [-\mathrm{j}k_{cc}(Z_{oe} - Z_{oo})\csc\theta]/2. \end{cases} \tag{4}$$

According to Chen CP et al. (2013), the transmission response of the symmetric structure can be precisely described by mode impedances Z_{oe}, Z_{oo}, and k_{cc}. Here, k_{cc} represents the ratio of the coupling coefficient of nonadjacent lines (k_{13}) to that of adjacent ones (k_{12}):

$$k_{cc} = k_{13}/k_{12}, \tag{5}$$

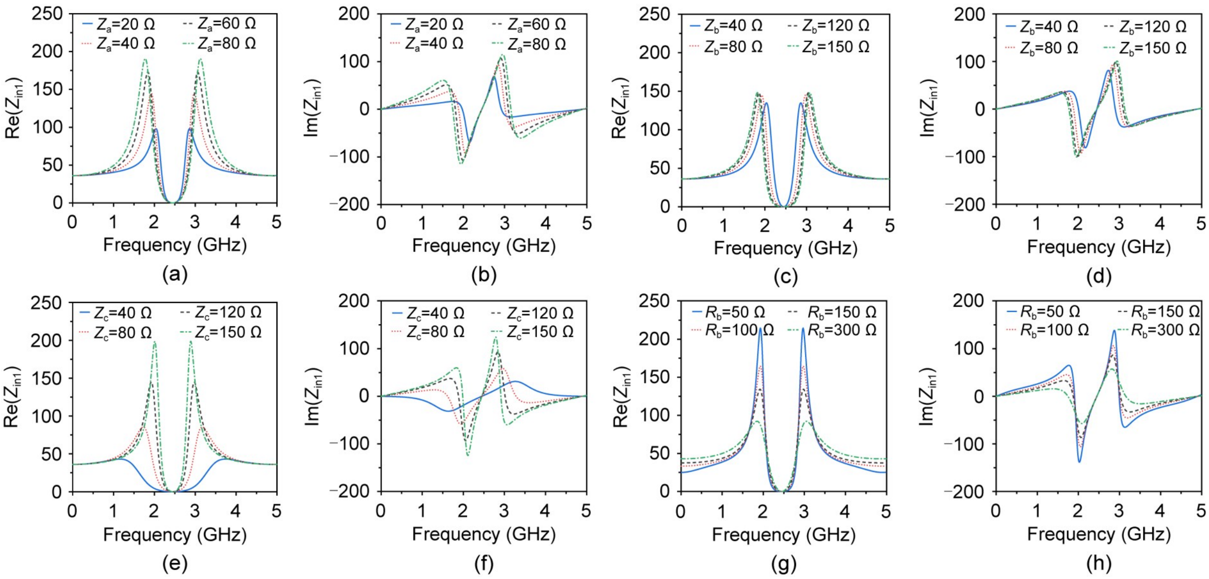

Fig. 5 Calculated Re(Z_{in1}) and Im(Z_{in1}) of the proposed absorptive section: (a–b) with various Z_a (Z_b=80 Ω, Z_c=120 Ω, R_b=150 Ω, R_a=50 Ω); (c–d) with various Z_b (Z_a=40 Ω, Z_c=120 Ω, R_b=150 Ω, R_a=50 Ω); (e–f) with various Z_c (Z_a=40 Ω, Z_b=80 Ω, R_b=150 Ω, R_a=50 Ω); (g–h) with various R_b (Z_a=40 Ω, Z_b=80 Ω, Z_c=120 Ω, R_a=50 Ω)

where k_{12} and k_{13} can be obtained by the parasitic coupling level (C in dB) (Chen JX et al., 2015) between two adjacent lines and two nonadjacent lines, respectively.

$$k_{12}, k_{13} \approx 10^{-\frac{C}{20}}. \tag{6}$$

The modal equations for the configuration of BPF section using TLCS shown in Fig. 6a can be derived as

$$I_2 = I_4 = I_6 = V_5 = 0, \tag{7a}$$
$$V_{\text{in}} = V_3, \tag{7b}$$
$$V_{\text{out}} = V_1, \tag{7c}$$
$$I_{\text{in}} = I_3, \tag{7d}$$
$$I_{\text{out}} = I_1, \tag{7e}$$

where V and I are the voltages and currents at ports, respectively. By substituting these conditions into Eqs. (3) and (4), the S-parameter matrix (S-matrix) of this two-port BPF can be directly extracted from the six-port Z-matrix as follows:

$$\begin{cases} S_{11} = \dfrac{m^2 - n^2 - Z_0^2}{m^2 - n^2 + Z_0^2 + 2mZ_0}, \\ S_{21} = \dfrac{2nZ_0}{m^2 - n^2 + Z_0^2 + 2mZ_0}, \end{cases} \tag{8}$$

where

$$\begin{cases} m = -\dfrac{\text{j}}{2}(Z_{\text{oe}} + Z_{\text{oo}})\cot\theta_{\text{c}} + \dfrac{\text{j}}{2}\dfrac{(Z_{\text{oe}} - Z_{\text{oo}})^2}{Z_{\text{oe}} + Z_{\text{oo}}}\dfrac{\csc^2\theta_{\text{c}}}{\cot\theta_{\text{c}}}, \\ n = -\dfrac{\text{j}}{2}k_{\text{cc}}(Z_{\text{oe}} - Z_{\text{oo}})\cot\theta_{\text{c}} + \dfrac{\text{j}}{2}\dfrac{(Z_{\text{oe}} - Z_{\text{oo}})^2}{Z_{\text{oe}} + Z_{\text{oo}}}\dfrac{\csc^2\theta_{\text{c}}}{\cot\theta_{\text{c}}}. \end{cases} \tag{9}$$

According to Eqs. (3)–(9), the calculated frequency response of the TLCS-based BPF is plotted in Fig. 6b. There are two transmission zeros (TZs) close to the passband due to the cross-coupling k_{13} of two nonadjacent CFLs ($k_{\text{cc}}\neq0$). Meanwhile, three transmission poles (TPs) are generated by the compact TLCS (Feng and Che, 2012), which expands the BW and improves the flatness of the passband, avoiding the requirement of multiple resonators. Furthermore, as shown in Fig. 7, the BW can be flexibly adjusted by w_{c} and s, and it becomes larger as w_{c} and s decrease. To further improve the roll-off skirt of the passband on the premise of ensuring passband flatness, an additional short stub loaded on the output port CFL, as shown in Fig. 8, is proposed. Fig. 9 invalidates that the roll-off skirt becomes steeper by this short stub (Z_{d}, θ_{d}). It can also enhance the flexibility to adjust the BW of the proposed BPF (BW_{BPF}, i.e., $|S_{21}|$>−3 dB) in Fig. 8.

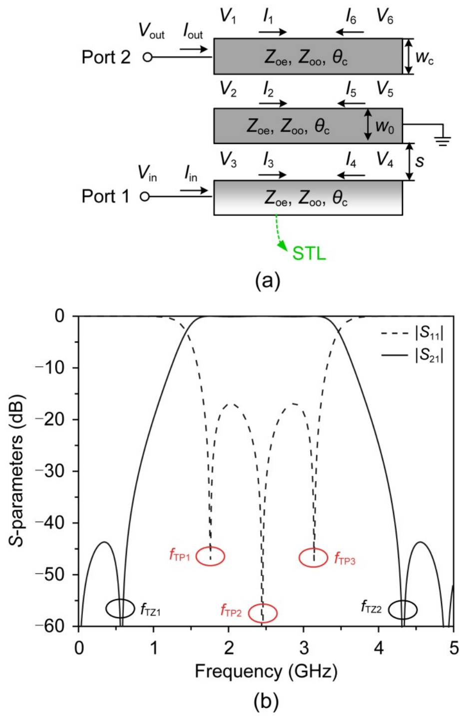

Fig. 6 Bandpass filter section using TLCS: (a) configuration; (b) calculated frequency response

2.1.3 Input-reflectionless differential-mode filter design

According to the above analysis, the STL is a key factor for determining the BW_{ABSS} and BW_{BPF} in this codesign. When Z_{c} in Fig. 4 increases, BW_{ABSS} decreases; in contrast, when w_{c} in Fig. 6a decreases (corresponding to the increase in Z_{c}), BW_{BPF} increases. To obtain good complementarity of ABSS and BPF section, BW_{BPF} can be tuned by s and Z_{d}, while BW_{ABSS} can be tuned by Z_{a} and Z_{b}. As a result, the proposed fusion design method shown in Fig. 3a can be easily realized to obtain miniaturization and good performance simultaneously.

For the DM bisected equivalent circuits of the proposed input-reflectionless balanced BPF shown in Fig. 3a, the $ABCD$ matrix of the DM bisected equivalent circuit can be obtained:

$$M_{\text{DM}} = \begin{bmatrix} A & B \\ C & D \end{bmatrix} = M_1 \times M_2, \tag{10}$$

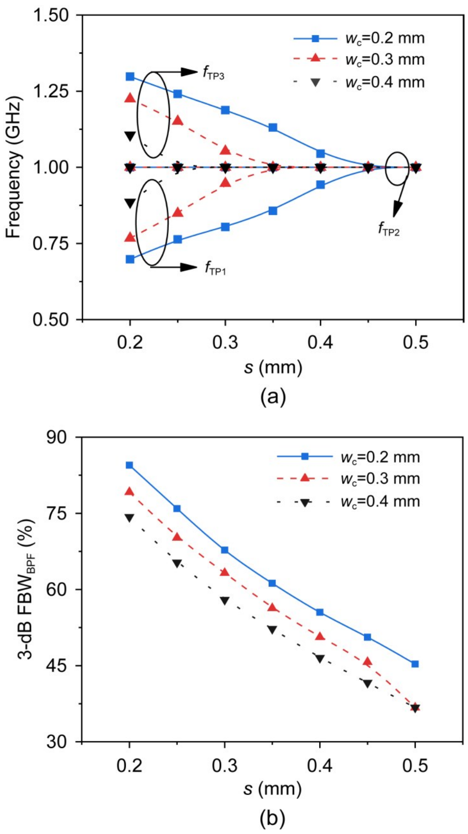

Fig. 7 TLCS-based bandpass filter design under different s and w_c with varied f_{TPs} (a) and 3-dB FBW_{BPF} (b)

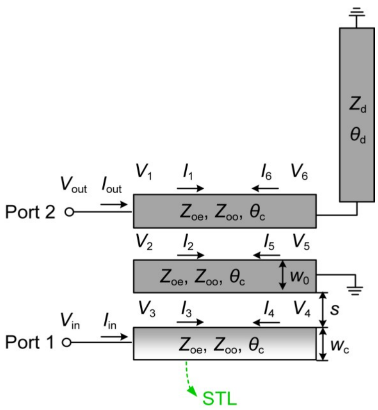

Fig. 8 Configuration of the TLCS-based bandpass filter with stub (Z_d, θ_d)

where M_1 is the *ABCD* matrix of the lossy stub (Z_a, θ_a, R_a), and M_2 is the *ABCD* matrix of the remaining part of the DM half circuits without a lossy stub (Z_a, θ_a, R_a). They can be expressed as follows (Pozar, 2012):

$$M_1 = \begin{bmatrix} 1 & 0 \\ 1/(R_a + jZ_a \tan\theta_a) & 1 \end{bmatrix}, \tag{11}$$

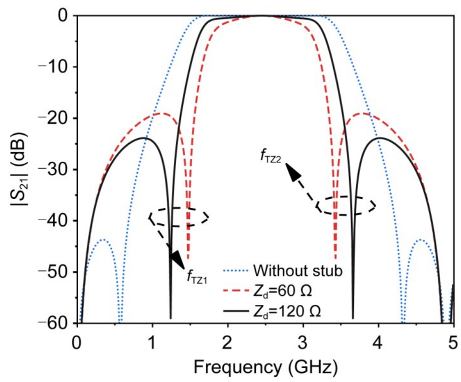

Fig. 9 Variation of frequency responses with/without stub (Z_d, θ_d) of the TLCS-based bandpass filter (Z_{oe}=175.2 Ω, Z_{oo}=63.3 Ω, k_{cc}=0.53)

$$M_2 = \begin{bmatrix} A_2 & B_2 \\ C_2 & D_2 \end{bmatrix}, \tag{12}$$

where M_2 can be obtained by substituting the conditions into Eqs. (3) and (4), and the conditions can be obtained as

$$I_2 = V_5 = 0, \tag{13a}$$

$$V_4 = -I_4(R_b + jZ_b \tan\theta_b), \tag{13b}$$

$$V_6 = -jI_6 Z_d \tan\theta_d. \tag{13c}$$

According to Eqs. (10)–(13), the S-matrix of the DM bisected equivalent circuit can be obtained as follows:

$$S_{11} = \frac{A + B/Z_0 - CZ_0 - D}{A + B/Z_0 + CZ_0 + D}, \tag{14}$$

$$S_{21} = \frac{2}{A + B/Z_0 + CZ_0 + D}. \tag{15}$$

Based on this, the calculated DM frequency response can be achieved.

Fig. 10 shows the good reflectionless performance when BW_{ABSS} is approximately equal to BW_{BPF}. Fusing these two parts by reusing the STL, the BW of the overall circuit (BW_{DM}, i.e., $|S_{dd21}|>-3$ dB) in Fig. 3a is smaller than BW_{BPF} and BW_{ABSS}. It is interesting to determine BW_{DM} by BW_{BPF} and BW_{ABSS}, which will be discussed below. At the same time, other performances, such as passband IL and absorption of both DM and CM, are evaluated. To facilitate the description of the resultant DM BPF, the BW ratio $\alpha = BW_{ABSS}/BW_{BPF}$ is defined. The calculated DM frequency responses under

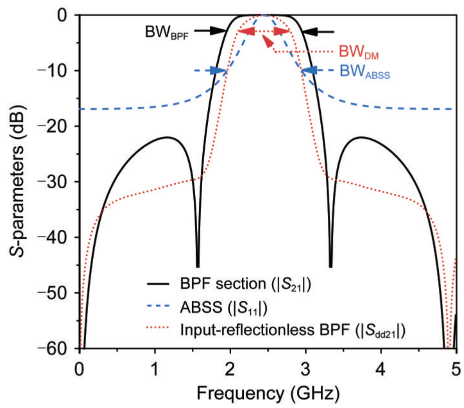

Fig. 10 Comparison between the calculated differential mode frequency response of the proposed input-reflectionless balanced BPF and the frequency responses of its ABSS and BPF section (Z_a=26 Ω, Z_b=60 Ω, Z_c=120 Ω, Z_d=120 Ω, R_a=50 Ω, R_b=150 Ω, Z_{oe}=151.7 Ω, Z_{oo}=80.5 Ω, k_{cc}=0.58)

different fractional BW_{ABSS} ($FBW_{ABSS}=BW_{ABSS}/f_0$) and FBW_{BPF} ($FBW_{BPF}=BW_{BPF}/f_0$) in Table 1, where α=1 is fixed, are plotted in Fig. 11. They show good reflectionless performances, as expected, which can be easily controlled by Z_a and Z_b of ABSS and Z_d and s (characterized by Z_{oe} and Z_{oo}) of the BPF section. From this, it can be concluded that BW_{DM} can be flexibly controlled by different BW_{ABSS} and BW_{BPF}. In conclusion, BW_{DM} is always less than BW_{BPF} or BW_{ABSS}, and as BW_{ABSS} and BW_{BPF} increase, BW_{DM} increases. As shown in Fig. 11, both DM passband flatness and reflectionless level are varied, which must be studied to optimize the overall performance of the DM filter.

To evaluate the effect of α, case 2 in Fig. 11 is chosen for study. Fig. 12 shows the calculated DM frequency responses of different cases in Table 2. When FBW_{BPF} is fixed at 40%, different values of α can be obtained by changing Z_a and Z_b of ABSS, and the other parameters are the same as those in case 2 in Table 1. The variable R_{max} marked in Fig. 12a is defined as the maximum reflection in the whole band. In addition, the variable PL in Table 2 is defined to quantitatively evaluate the passband flatness (i.e., distortion at the edges of the passband). The larger the PL, the worse the flatness. PL can be given as follows:

$$PL = \frac{3\text{-dB } BW_{DM}}{1\text{-dB } BW_{DM}}, \tag{16}$$

where 3-dB BW_{DM} (i.e., BW_{DM}) and 1-dB BW_{DM} (i.e., $|S_{dd21}|>-1$ dB) can be obtained from Fig. 12b. Thus, the reflectionless performance and passband performance of the proposed input-reflectionless balanced BPF can be represented by R_{max} and PL, respectively. The curves of R_{max} and PL under different α values are plotted in Fig. 13. It shows that the balance between reflectionless performance and passband performance can be adjusted by α. According to the above analysis, the following can be concluded:

1. BW_{DM} is flexibly controlled by BW_{BPF} and BW_{ABSS}. Regardless of the value of α, BW_{DM} is smaller than BW_{BPF} and BW_{ABSS}.

Table 1 Parameters of the input-reflectionless balanced BPFs (α = 1)

Case	FBW_{ABSS} (%)	FBW_{BPF} (%)	3-dB FBW_{DM} (%)	Z_a (Ω)	Z_b (Ω)	Z_c (Ω)	Z_d (Ω)	R_a (Ω)	R_b (Ω)	Z_{oe} (Ω)	Z_{oo} (Ω)	k_{cc}
1	21.2	21.2	12.24	20	25	120	120	50	150	139.1	94.9	0.66
2	40.0	40.0	28.57	26	60	120	120	50	150	151.7	80.5	0.58
3	66.1	66.1	44.89	38	78	120	120	50	150	166.6	61.5	0.52

Table 2 Parameters of the input-reflectionless balanced BPFs with different α

Case	FBW_{BPF} (%)	α	FBW_{ABSS} (%)	3-dB FBW_{DM} (%)	1-dB FBW_{DM} (%)	PL	R_{max} (dB)	Z_a (Ω)	Z_b (Ω)
2a	40	0.5	20.4	15.51	7.35	2.11	−11.74	20	20
2b	40	0.75	30	24.08	13.22	1.82	−16.22	24	40
2	40	1	40	28.57	17.96	1.59	−16.90	26	60
2c	40	1.25	50	31.43	21.38	1.47	−15.95	30	75
2d	40	1.5	60	32.24	23.27	1.38	−13.07	36	80
2e	40	1.75	70	33.31	24.89	1.34	−11.19	40	90
2f	40	2	80	34.28	26.53	1.29	−9.45	45	100

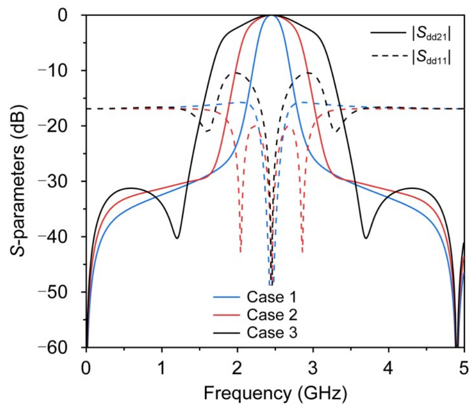

Fig. 11 Calculated differential mode frequency responses of different cases in Table 1 (α=1 is fixed) (References to color refer to the online version of this figure)

2. When α=1 (e.g., case 2), input-reflectionless balanced BPF shows a good reflectionless performance (R_{max}=−16.90 dB, which is the optimal value in the interval 0.5–2 of α), and PL=1.59.

3. When α<1, as α decreases from 1 to 0.5 in case 2a, R_{max} increases to −11.74 dB, which manifests a degradation of the reflectionless performance. Moreover, as shown in Fig. 12b, the passband produces severe distortion, which is characterized by PL=2.11.

4. When α>1, the reflectionless performance around the passband is affected. When α=1.5 in case 2d, there is a slight effect on the reflectionless performance (R_{max}=−13.07 dB), but the passband performance (PL=1.38) is improved. However, when α=2 in case 2f, the reflectionless performance deteriorates sharply (R_{max}=−9.45 dB), although its passband performance is enhanced (PL=1.29).

5. In summary, when α increases from 0.5 to 1, R_{max} decreases from −11.74 dB to −16.90 dB, while when α increases from 1 to 2, R_{max} increases from −16.90 dB to −9.45 dB. In addition, PL decreases as α increases, which means that the larger α is, the flatter the passband is. According to Fig. 13, to obtain a good compromise between reflectionless performance (R_{max}<−10 dB) and passband performance (PL<1.5), the optimal interval for α is 1.2–1.9.

In addition, the BW_{DM} and α are determined by the parameters Z_a, Z_b, Z_c, Z_d, Z_{oe}, Z_{oo}, and k_{cc}. R_b in Fig. 3a can also be used to further optimize the reflectionless performance of the proposed filter. According to Fig. 14, although the matching performance of the ABSS near f_0 and at the second harmonic ($2f_0$) is

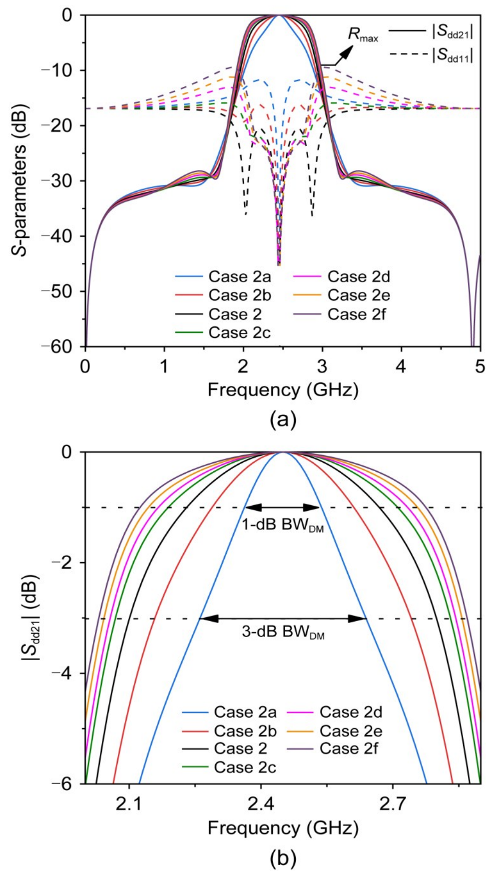

Fig. 12 Calculated differential mode frequency responses of different cases in Table 2: (a) transfer coefficient ($|S_{dd21}|$) and reflection coefficient ($|S_{dd11}|$); (b) $|S_{dd21}|$ (BW_{BPF} is fixed as 40% with some parameters being the same as in case 2: Z_{oe}=151.7 Ω, Z_{oo}=80.5 Ω, Z_d=120 Ω, k_{cc}=0.58, Z_c=120 Ω, R_a=50 Ω, R_b=150 Ω) (References to color refer to the online version of this figure)

improved by increasing R_b, as in Figs. 5g and 5h, with the varied R_b, passband and reflectionless performances have opposite variation trends, and thus a trade-off is needed. Specifically, as R_b increases from 50 Ω to 300 Ω, the reflectionless performance increases (R_{max} decreases from −5.86 dB to −16.72 dB), but PL increases from 1.19 to 1.56. Accordingly, considering a good compromise between reflectionless performance and passband performance, the range of R_b is 50–150 Ω.

Through the above analysis, the BW_{ABSS} and BW_{BPF} of the proposed input-reflectionless balanced BPF can be easily adjusted to achieve flexible BW_{DM}, and the BW ratio α is a significant indicator to achieve both wideband DM absorption and good passband performance. In addition, the performance can be easily optimized by the codesign method.

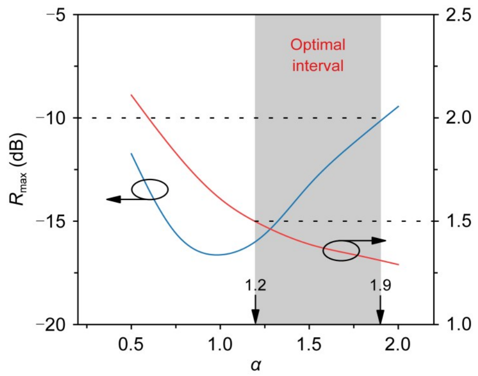

Fig. 13 Performance of the proposed input-reflectionless balanced BPF with varied α in Table 2 (R_{max} and PL)

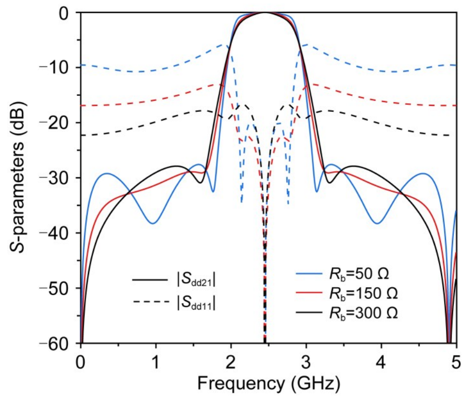

Fig. 14 Calculated differential mode frequency responses of case 2d with varied R_b (References to color refer to the online version of this figure)

2.2 Common mode analysis

When the CM excitation is applied to the proposed input-reflectionless balanced BPF in Fig. 2, the symmetrical plane AA' is equivalent to a magnetic wall. Thus, the CM bisected equivalent circuit can be obtained, as shown in Fig. 3b. To obtain wideband CM absorption performance, the absorption behavior at both DC and $2f_0$ is a key indicator. At DC and $2f_0$, the $\lambda/4$ open stubs (Z_b and Z_d) and the absorption resistor R_b loaded in the terminal of CFLs can be regarded as transparent, so that most CM noise can be absorbed by the absorption resistor R_a. Thus, when $R_a=Z_0$, the ideal absorption behavior at both DC and $2f_0$ can be obtained. Meanwhile, R_b in Fig. 3b can be used to optimize CM absorption and suppression levels. The calculated CM frequency responses with the same parameters as in case 2d with varied R_b are plotted in Fig. 15. As R_b increases, the CM absorption level increases,

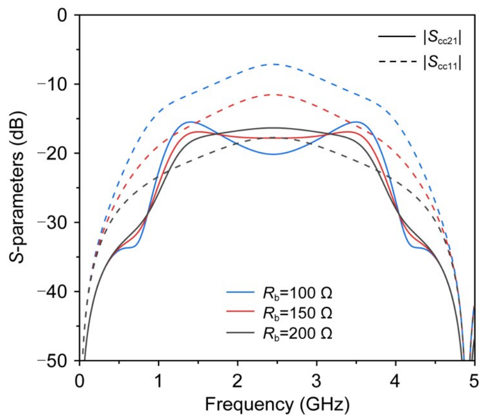

Fig. 15 Calculated common mode frequency responses of case 2d with varied R_b (References to color refer to the online version of this figure)

but the suppression level at f_0 worsens. Considering a good balance between the CM suppression level and CM absorption performance, and combined with the requirement of DM reflectionless performance, the final optimization range of R_b is 100–150 Ω.

To summarize the above DM and CM analysis, the main design procedure of the proposed input-reflectionless balanced BPF is as follows:

1. Determine the center frequency f_0 and BW_{DM}. According to Fig. 10, the relationship between BW_{DM} and BW_{BPF} is $BW_{BPF}>BW_{DM}$. On this basis, the approximate BW_{BPF} can be determined from different cases in Table 1, and it can be easily achieved by adjusting s and Z_d of the BPF section.

2. Considering the balance between the DM reflectionless performance and passband performance, α can be determined according to the curves of R_{max} and PL versus α shown in Fig. 13.

3. Once BW_{DM}, BW_{BPF}, and α are determined, BW_{ABSS} can be determined. This can be easily achieved by adjusting the Z_a and Z_b of the ABSS.

4. Adjust R_b to obtain a wideband DM and CM reflectionless behavior, minimize DM passband distortion, and improve the CM suppression level. Then, the optimal range of R_b (100–150 Ω) can be obtained.

5. After the initial impedance parameters are obtained by the above design procedure, the proposed input-reflectionless balanced BPF can be constructed and further optimized by the full-wave High-Frequency Structure Simulator (HFSS) once the physical dimensions are converted by Line Calc calculation in the Advanced Design System (ADS).

3 Implementation and discussion

For demonstration, the proposed TLCS-based input-reflectionless balanced BPF is fabricated on a Rogers RO4003 substrate with a relative dielectric constant ε_r=3.55, dielectric loss tan δ=2.7×10^{-3}, dielectric thickness h=0.813 mm, and metallization thickness t= 0.035 mm. The center frequency f_0 is set at 2.45 GHz. The design specification of the ripple FBW$_{DM}$=32% is prescribed for the proposed input-reflectionless balanced BPF. With the selected BW ratio α=1.5 and FBW$_{BPF}$=40%, FBW$_{ABSS}$ is 60%. Based on this, the optimized parameters (Z_a=36 Ω, Z_b=80 Ω, Z_c=115 Ω, Z_d=125 Ω, R_a=50 Ω, R_b=130 Ω) can be easily obtained according to the design procedure in Section 2.2.

Then, the physical model can be built on HFSS, and the layout can be optimized. The photograph and layout of the proposed filter are shown in Fig. 16. The simulation is performed with HFSS, and the measurement is conducted by the Agilent N5230A network analyzer, which is a four-port network analyzer that can be used to measure the balanced circuits directly. The measured S-parameters are plotted in Fig. 17 along with the simulation results for comparison. Although the differences between the simulation and measurement results, such as |S_{dd11}| and |S_{cc11}|, can be observed at approximately 6 GHz, the fractional absorption BWs of both DM and CM in the simulation and measurement are almost the same. The largest deviation comes from the simulated and measured |S_{dd11}|, which would be caused by the manufacturing tolerances (e.g., dielectric constant of the employed substrate and implementation of the demonstration board). Overall, the differences between the results in Fig. 17 are acceptable.

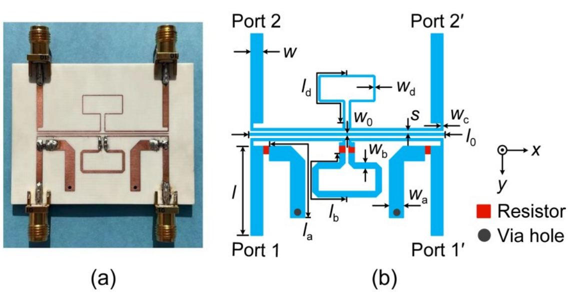

Fig. 16 Implementation of the proposed input-reflectionless balanced bandpass filter: (a) photograph; (b) layout (l= 18 mm, l_0=19.25 mm, l_a=19.85 mm, l_b=19.29 mm, l_d=20.3 mm, w=1.78 mm, w_0=0.2 mm, w_a=2.9 mm, w_b=0.74 mm, w_c= 0.28 mm, w_d=0.2 mm, s=0.44 mm)

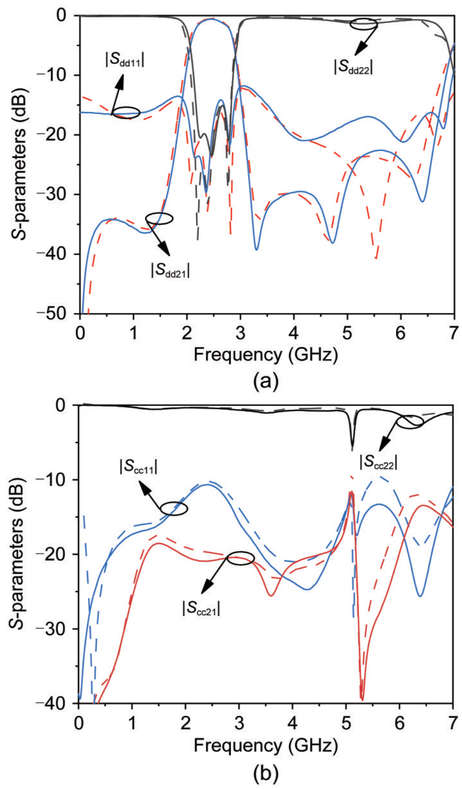

Fig. 17 Simulation (dashed lines) and measurement (solid lines) results of the proposed input-reflectionless balanced BPF: (a) differential mode; (b) common mode (References to color refer to the online version of this figure)

For the DM shown in Fig. 17a, the measured FBW$_{DM}$ is approximately 31.4%. Meanwhile, the DM absorptive BW is 285.7%, and the minimum in-band IL (IL$_{min}$) is 0.43 dB. The improved roll-off skirt is obtained by four TZs, which are located at 0, 1.28, 3.28, and 4.72 GHz. Moreover, the rejection levels of over 20 dB at the upper stopband extend to 6.65 GHz (2.72f_0). For the CM shown in Fig. 17b, it is noted that the absorptive BW is also in a wide range (DC to 7 GHz, 285.7%), and over 18.4 dB CM suppression (|S_{cc21}|) is achieved from DC to 4.9 GHz (2f_0).

Comparisons with previous reflectionless differential BPFs are summarized in Table 3. Gómez-García et al. (2018) and Yang et al. (2020) did not consider the absorption of the reflected CM noise, which is a key factor for stabilizing the RF system. Moreover, due to the cascaded topology in Gómez-García et al. (2018) and the multi-layered vertical transition structure in Yang et al. (2020), the circuit sizes are large. Some efforts have been made to consider the absorption of unwanted DM and CM signals (Chen X et al.,

Table 3 Comparisons with previous reflectionless differential bandpass filters

Reference	f_0 (GHz)/ n_{TZ}	FBW_{DM} (%)/ IL_{min} (dB)	$\|S_{dd11}\|$ absorptive BW (%)	$\|S_{cc11}\|$ absorptive BW (%)	DM stopband*	Size ($\lambda\times\lambda$)	Orders
Gómez-García et al., 2018	3.04/2	21.8/0.60	65.8	N/A	$1.15f_0$	2.35×1.60	2
Yang et al., 2020	1.92/4	65.5/0.50	260.0	N/A	$2.75f_0$	1.23×0.48	4
Zhang YF et al., 2022	1.98/4	40.0/0.65	275.0	200.0	$2.02f_0$	0.73×0.53	3
Chen X et al., 2021	2.15/2	15.8/1.00	222.0	188.8	$2.79f_0$	1.19×0.37	3
This work	2.45/4	31.4/0.43	285.7	285.7	$2.72f_0$	0.52×0.36	3

n_{TZ}: number of transmission zeros. $|S_{dd11}|$ and $|S_{cc11}|$ absorptive BW (%) are defined as the percentage of $|S_{dd11}|<-10$ dB and $|S_{cc11}|<-10$ dB to the center frequency (f_0), respectively. * The rejection level is over 20 dB

2021; Zhang YF et al., 2022). DM absorptive BW is approximately 275%, and the CM absorptive BW reaches 200% (Zhang YF et al., 2022). However, its DM upper stopband BW is limited due to the use of the $\lambda/2$ coupled ring resonator. In contrast, the proposed filter with a wider upper stopband for DM is due to the adoption of the TLCS. To extend the absorptive BW for the DM and CM, the cascading design is used, resulting in an enlarged circuit size and high IL (Chen X et al., 2021). As seen from Table 3, the proposed input-reflectionless balanced BPF has a more compact circuit layout due to the syncretic working mechanism and the adoption of TLCS. Meanwhile, the proposed filter exhibits larger DM and CM absorptive BWs and lower IL_{min} due to the design guidelines derived from the detailed analysis. In conclusion, the proposed differential filter exhibits remarkable DM and CM reflectionless performance and filtering performance under the premise of a compact layout.

4 Conclusions

In this paper, a compact input-reflectionless balanced bandpass filter with a flexible bandwidth is presented. It features an innovative conception of the fusion design, especially reusing the shared transmission lines of the absorptive section and bandpass filter section, resulting in a miniaturized circuit and low insertion loss. Meanwhile, the three-line coupled structure introduces the miniaturization of the bandpass filter section with three controllable transmission poles, so that BW_{BPF} can be easily controlled. In addition, BW_{ABSS} and BW_{BPF} can be adjusted independently, which is helpful for obtaining flexible BW_{DM}, so that the specifications of the differential mode reflectionless filter can be realized in practical applications. In conclusion, the proposed input-reflectionless balanced bandpass filter caters to the development trend of miniaturization and high performance of wireless communication equipment, while eliminating the common mode and differential mode reflected interference signals that are common in the traditional balanced bandpass filter, and is an attractive choice for the radio frequency front end of the wireless communication system.

Contributors

Yahui ZHU designed the research, processed the data, and drafted the paper. Jing CAI, Wei QIN, Wenwen YANG, and Jianxin CHEN helped organize the paper. Yahui ZHU and Jianxin CHEN revised and finalized the paper.

Compliance with ethics guidelines

Yahui ZHU, Jing CAI, Wei QIN, Wenwen YANG, and Jianxin CHEN declare that they have no conflict of interest.

Data availability

The data that support the findings of this study are available from the corresponding author upon reasonable request.

References

Bi XJ, Zeng X, Xu QF, 2020. Slotline-based balanced filter with ultra-wide stopband and high selectivity. *IEEE Trans Circ Syst II Exp Briefs*, 67(3):460-464. https://doi.org/10.1109/TCSII.2019.2914072

Cao YF, Zhang Y, Zhang XY, 2020. Filtering antennas: from innovative concepts to industrial applications. *Front Inform Technol Electron Eng*, 21(1):116-127. https://doi.org/10.1631/FITEE.1900474

Chen CP, Oda J, Kamata K, et al., 2013. An iterative synthesis scheme for wideband filter based on parallel-coupled three-line. IEEE European Microwave Conf, p.889-892. https://doi.org/10.23919/EuMC.2013.6686800

Chen JX, Zhan Y, Xue Q, 2015. Novel LTCC distributed-element wideband bandpass filter based on the dual-mode stepped-impedance resonator. *IEEE Trans Compon Packag Manuf*

Technol, 5(3):372-380.
https://doi.org/10.1109/TCPMT.2015.2401023

Chen JX, Zhan Y, Qin W, et al., 2016. Analysis and design of balanced dielectric resonator bandpass filters. *IEEE Trans Microw Theory Techn*, 64(5):1476-1483.
https://doi.org/10.1109/TMTT.2016.2546260

Chen X, Yang T, Chi PL, 2021. Arbitrary-order balanced filter with reflectionless characteristics for both common- and differential-mode signals. *IEEE Microw Wirel Compon Lett*, 31(6):553-556. https://doi.org/10.1109/LMWC.2021.3068469

Fan MY, Song KJ, Yang L, et al., 2021a. Frequency-reconfigurable input-reflectionless bandpass filter and filtering power divider with constant absolute bandwidth. *IEEE Trans Circ Syst II Exp Briefs*, 68(7):2424-2428.
https://doi.org/10.1109/TCSII.2021.3049417

Fan MY, Song KJ, Yang L, et al., 2021b. Frequency-tunable constant-absolute-bandwidth single-/dual-passband filters and diplexers with all-port-reflectionless behavior. *IEEE Trans Microw Theory Techn*, 69(2):1365-1377.
https://doi.org/10.1109/TMTT.2020.3040481

Feng WJ, Che WQ, 2012. Wideband balanced bandpass filter based on three-line coupled structure. *Electron Lett*, 48(16): 1006-1008. https://doi.org/10.1049/el.2012.0448

Feng WJ, Che WQ, Shi YR, et al., 2019. Balanced rat-race couplers with wideband common-mode suppression. *IEEE Trans Microw Theory Techn*, 67(12):4724-4732.
https://doi.org/10.1109/TMTT.2019.2946158

Feng WJ, Pan BS, Zhu HS, et al., 2021. High performance balanced bandpass filters with wideband common mode suppression. *IEEE Trans Circ Syst II Exp Briefs*, 68(6): 1897-1901. https://doi.org/10.1109/TCSII.2020.3044092

Gómez-García R, Muñoz-Ferreras JM, Psychogiou D, et al., 2018. Balanced symmetrical quasi-reflectionless single-and dual-band bandpass planar filters. *IEEE Microw Wirel Compon Lett*, 28(9):798-800.
https://doi.org/10.1109/LMWC.2018.2856400

Gómez-García R, Muñoz-Ferreras JM, Psychogiou D, 2019. Symmetrical quasi-absorptive RF bandpass filters. *IEEE Trans Microw Theory Techn*, 67(4):1472-1482.
https://doi.org/10.1109/TMTT.2019.2895531

Guilabert A, Morgan MA, Boyd TA, 2019. Reflectionless filters for generalized elliptic transmission functions. *IEEE Trans Circ Syst I Reg Papers*, 66(12):4606-4618.
https://doi.org/10.1109/TCSI.2019.2931469

Han Y, Chang YM, Che WQ, 2022. Frequency-selective rasorbers: a view of frequency-selective rasorbers and their application in reducing the radar cross sections of antennas. *IEEE Microw Mag*, 23(2):86-98.
https://doi.org/10.1109/MMM.2021.3125463

Kou N, Yu SX, Ding Z, et al., 2022. Monopulse transmitarray antenna fed by aperture-coupled microstrip structure. *Front Inform Technol Electron Eng*, 23(3):502-510.
https://doi.org/10.1631/FITEE.2000547

Lee B, Lee JH, Lee G, et al., 2022. All-port-reflectionless narrowband filtering power divider topology with generic equations. *IEEE Trans Circ Syst I Reg Papers*, 69(4):1417-1426. https://doi.org/10.1109/TCSI.2021.3133585

Lee J, Lee JH, Barker NS, 2021. Rigorous design of input-reflectionless filter with Chebyshev response and exact approach to increase reflectionless range. *IEEE Trans Microw Theory Techn*, 69(10):4460-4475.
https://doi.org/10.1109/TMTT.2021.3098530

Li HY, Xu JX, Zhang XY, 2019. Substrate integrated waveguide filtering rat-race coupler based on orthogonal degenerate modes. *IEEE Trans Microw Theory Techn*, 67(1):140-150. https://doi.org/10.1109/TMTT.2018.2874252

Li YC, Wu DS, Xue Q, et al., 2020. Miniaturized single-ended and balanced dual-band diplexers using dielectric resonators. *IEEE Trans Microw Theory Techn*, 68(10):4257-4266.
https://doi.org/10.1109/TMTT.2020.3008784

Lin TY, Wu TL, 2020. Balanced bandpass filter with common-mode reflectionless feature by terminated coupled lines. *IEEE Trans Electromagn Compat*, 62(4):1090-1097.
https://doi.org/10.1109/TEMC.2020.2991715

Lin TY, Huang YC, Wu TL, 2019. Novel absorptive balanced bandpass filters using resistive loaded transmission lines. *IEEE Trans Compon Packag Manuf Technol*, 9(4):745-753.
https://doi.org/10.1109/TCPMT.2018.2861428

Morgan MA, Boyd TA, 2015. Reflectionless filter structures. *IEEE Trans Microw Theory Techn*, 63(4):1263-1271.
https://doi.org/10.1109/TMTT.2015.2403841

Morgan MA, Groves WM, Boyd TA, 2019. Reflectionless filter topologies supporting arbitrary low-pass ladder prototypes. *IEEE Trans Circ Syst I Reg Papers*, 66(2):594-604.
https://doi.org/10.1109/TCSI.2018.2872424

Pozar DM, 2012. Microwave Engineering (4^{th} Ed.). New York, USA, p.188-190.

Shi J, Xu K, Zhang W, et al., 2016. An approach to 1-to-2^n way microstrip balanced power divider. *IEEE Trans Microw Theory Techn*, 64(12):4222-4231.
https://doi.org/10.1109/TMTT.2016.2611495

Song KJ, Yao JC, Chen YX, et al., 2020. Balanced diplexer based on substrate integrated waveguide dual-mode resonator. *IEEE Trans Microw Theory Techn*, 68(12):5279-5287. https://doi.org/10.1109/TMTT.2020.3015968

Wang XY, Tang SC, Chen JX, 2022. Differential-fed pattern-reconfigurable dielectric patch antenna and array with low cross-polarization. *IEEE Trans Antenn Propag*, 70(5):3870-3875. https://doi.org/10.1109/TAP.2021.3125363

Wu DS, Li YC, Xue Q, et al., 2022. Balanced dielectric resonator filters with multiple reconfigurable passbands. *IEEE Trans Microw Theory Techn*, 70(1):180-189.
https://doi.org/10.1109/TMTT.2021.3081989

Wu XH, Li YS, Liu XG, 2020. High-order dual-port quasi-absorptive microstrip coupled-line bandpass filters. *IEEE Trans Microw Theory Techn*, 68(4):1462-1475.
https://doi.org/10.1109/TMTT.2019.2955692

Xu KD, Bai YC, Ren X, et al., 2019. Broadband filtering power dividers using simple three-line coupled structures. *IEEE Trans Compon Packag Manuf Technol*, 9(6):1103-1110.
https://doi.org/10.1109/TCPMT.2018.2869077

Xu KD, Lu S, Guo YJ, et al., 2022. Quasi-reflectionless filters using simple coupled line and T-shaped microstrip structures. *IEEE J Radio Freq Identif*, 6(1):54-63.

https://doi.org/10.1109/JRFID.2021.3106664

Yamamoto S, Azakami T, Itakura K, 1966. Coupled strip transmission line with three center conductors. *IEEE Trans Microw Theory Techn*, 14(10):446-461. https://doi.org/10.1109/TMTT.1966.1126304

Yang L, Gómez-García R, Fan MY, 2020. Input-reflectionless balanced wideband bandpass filter using multilayered vertical transitions. IEEE Asia-Pacific Microwave Conf, p.443-449. https://doi.org/10.1109/APMC47863.2020.9331419

Yu W, Xu L, Zhang XY, et al., 2022. Dual-band dual-mode dielectric resonator filtering power divider with flexible output phase difference and power split ratio. *IEEE Trans Microw Theory Techn*, 70(1):190-199. https://doi.org/10.1109/TMTT.2021.3113654

Zhang WW, Wu YL, Liu YA, et al., 2017. Planar wideband differential-mode bandpass filter with common-mode noise absorption. *IEEE Microw Wirel Compon Lett*, 27(5):458-460. https://doi.org/10.1109/LMWC.2017.2690839

Zhang YF, Wu YL, Wang WM, et al., 2022. High-performance common- and differential-mode reflectionless balanced band-pass filter using coupled ring resonator. *IEEE Trans Circ Syst II Exp Briefs*, 69(3):974-978. https://doi.org/10.1109/TCSII.2021.3103535

Zhang ZQ, Zhang B, Li DT, et al., 2021. A mechanical reliability study of 3-dB waveguide hybrid couplers in submillimeter and terahertz bands. *Front Inform Technol Electron Eng*, 22(8):1104-1113. https://doi.org/10.1631/FITEE.2000229

Zhou WJ, Chen JX, 2017. High-selectivity tunable balanced bandpass filter with constant absolute bandwidth. *IEEE Trans Circ Syst II Exp Briefs*, 64(8):917-921. https://doi.org/10.1109/TCSII.2016.2621120

Zhu Y, Song KJ, Fan MY, et al., 2020. Wideband balanced bandpass filter with common-mode noise absorption using double-sided parallel-strip line. *IEEE Microw Wirel Compon Lett*, 30(4):359-362. https://doi.org/10.1109/LMWC.2020.2974089

Zhu YH, Cai J, Chen JX, 2022. Quasi-reflectionless double-sided parallel-strip line bandpass filter with enhanced selectivity. *IEEE Trans Circ Syst II Exp Briefs*, 69(2):339-343. https://doi.org/10.1109/TCSII.2021.3099508